# Holmium phosphate nanoparticles as negative contrast agents for high-field magnetic resonance imaging: Synthesis, magnetic relaxivity study and in vivo evaluation.

E. Gómez-González,[1] Carlos Caro,[2] D. Martínez-Gutiérrez,[1] María L. García-Martín,[2] M. Ocaña[1] and A. I. Becerro[1*]

[1]*Instituto de Ciencia de Materiales de Sevilla (CSIC-US). c/Américo Vespucio, 49, 41092 Seville, Spain*

[2]*BIONAND, Andalusian Centre for Nanomedicine and Biotechnology (Junta de Andalucía–Universidad de Málaga) and CIBER-BBNMálaga 29590, Spain*
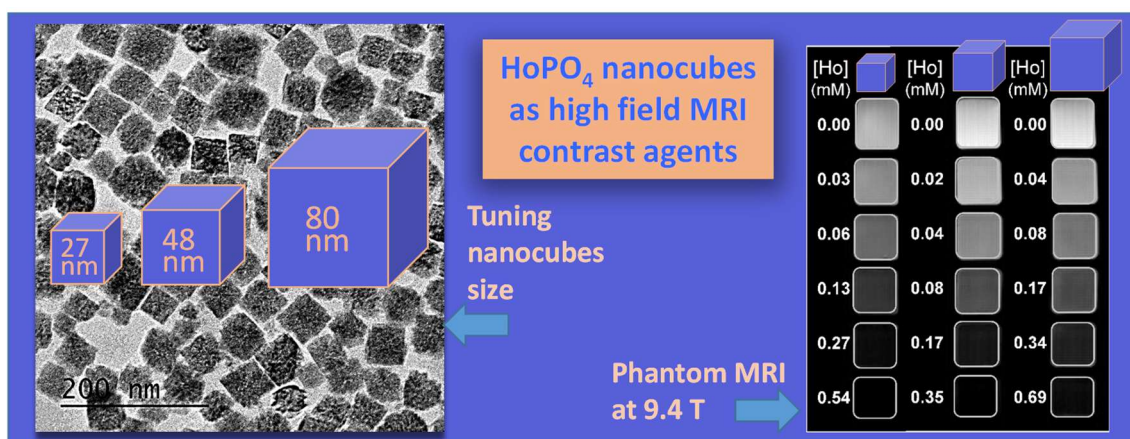
*Corresponding author. E-mail address: anieto@icmse.csic.es

Abstract

The increasing use of high magnetic fields in magnetic resonance imaging (MRI) scanners demands new contrast agents, since those used in low field instruments are not effective at high fields. In this paper, we report the synthesis of a negative MRI contrast agent consisting of $HoPO_4$ nanoparticles (NPs). Three different sizes (27 nm, 48 nm and 80 nm) of cube-shaped nanoparticles were obtained by homogeneous precipitation in polyol medium and then coated with poly(acrylic) acid (PAA) to obtain stable colloidal suspensions of $HoPO_4$@PAA NPs in physiological medium (PBS). The transverse relaxivity (r_2) of aqueous suspensions of the resulting NPs was evaluated at both 1.5 T and 9.4 T. A positive correlation between r_2 values and field strength as well as between r_2 values and particle size at both magnetic field strengths was found although this correlation failed for the biggest NPs at 9.4 T, likely due to certain particles aggregation inside the magnet. The highest r_2 value (489.91 $mM^{-1}s^{-1}$) was found for the 48 nm NPs at 9.4 T. Toxicity studies demonstrated that the latter NPs exhibited low toxicity to living systems. Finally, *in vivo* studies demonstrated that $HoPO_4$@PAA NPs could be a great platform for next-generation T_2-weighted MRI contrast agents at high magnetic field.

1. Introduction

Magnetic resonance imaging (MRI) is one of the most commonly used clinical diagnostic techniques to get morphological and functional images of organs and tissues. Although it provides a high spatial resolution, one of the main disadvantages of MRI is its low sensitivity, which has partially been overcome using contrast agents (CAs). MRI CAs increase the water proton relaxation rate of the tissues and organs where the CA is bio-distributed, the most well-known MRI CAs currently used in clinics being Gd-chelates.[1] Gd-based inorganic NPs (NPs) have also been largely investigated as MRI CAs because they present interesting advantages over Gd-chelates such as a drastic increase in the Gd ion concentration at nanoparticle surface, available for water interaction, easy functionalization and bioconjugation, which allows for targeting control, and release through particle size.[2,3,4] Gd-based CAs are known as positive MRI CAs because they cause brightening contrasting effect in T_1-weighted MR images as they shorten the longitudinal relaxation time (T_1) of water protons. Superparamagnetic iron oxide (SPIO) NPs are another type of MRI CAs that shorten the transverse relaxation time (T_2) of water protons, thus producing darkening in T_2-weighted MR images.[5]

The clinical magnets in use today in MRI are in the 0.5-Tesla to 3.0-Tesla range. Increasing the magnetic field strength to values higher than 3 T has been demonstrated to enhance the sensitivity of the MRI technique, as it results in better signal-to-noise ratio and greater spatial/temporal resolution. The MRI CAs mentioned above show efficient contrast enhancement at low magnetic field strengths (<1.5 T) but they are less effective at high magnetic fields. For example, the optimum magnetic field strength for Gd^{3+} chelates (T_1 MRI CAs) is <1 T and SPIO (T_2 MRI CA) suffers magnetization saturation at 1.5 T.[6,7] It is, therefore, challenging to find MRI CAs that show optimum contrast at high magnetic fields.

The unpaired electrons in Ln^{3+} ions other than Gd^{3+} populate the f orbitals anisotropically, which results in a strong magnetic anisotropy and fast electronic relaxation.[8] The relaxation enhancement of these metal ions can have significant contribution from the Curie-spin relaxation mechanism, which increases with the square of the magnetic field and primarily influences T_2.[9] Curie-spin relaxation becomes an especially important relaxation mechanism in compounds of certain lanthanide ions (e.g., Tb^{3+}, Dy^{3+}, Ho^{3+} and Er^{3+}) because of their high magnetic moments.[10] Among them, Dy^{3+} and Ho^{3+} show the highest magnetic moment values, which has led to the publication of a number of studies

about Dy^{3+}- and Ho^{3+}-based chelates[11,12,13] and inorganic NPs[14,15,16,17,18,19,20,21,22,23] as MRI CAs at high magnetic fields. Inorganic NPs show interesting advantages over chelates that were already described above for the Gd case. The vast majority of the studies using Dy^{3+}- and Ho^{3+}-NPs were conducted on fluoride matrices. Lanthanide phosphates show, however, several advantages over lanthanide fluorides, namely their lower water solubility[24,25] and higher biocompatibility.[26] However, to the best of our knowledge, the magnetic properties of $HoPO_4$ nanometer-size particles as MRI CA at high magnetic field have not been reported. The lack of literature on this important subject could be due to the fact that no synthesis method has been described so far for the fabrication of uniform $HoPO_4$ particles with nanometer dimensions.

In this study, we report a simple synthesis method, based on a homogeneous precipitation reaction in polyol medium, to obtain uniform, nanometer size $HoPO_4$ particles. The method renders cubic-like $HoPO_4$ NPs whose size can be tuned in the 27 nm – 80 nm range through the variation of the phosphoric acid concentration used as phosphate precursor. The morphology and crystal structure of the as-prepared NPs were analyzed by means of transmission electron microscopy and X-ray diffraction. The NPs surface was then functionalized with polyacrylic acid to increase their colloidal stability in phosphate buffered saline (PBS) and the transverse and longitudinal magnetic relaxivity values of the functionalized NPs were evaluated as a function of particle size. Then, cytotoxicity was thoroughly assessed in cell cultures by different methods, including MTT assay, life-dead assay, and flow cytometry. Finally, *in vivo* studies in mice were conducted to evaluate the applicability of $HoPO_4$ NPs as high field MRI contrast agents.

2. Experimental Section

2.1. Materials

Holmium acetate hydrate ($Ho(CH_3COO)_3 \cdot xH_2O$, Sigma Aldrich, 99.99%) and holmium nitrate hydrate ($Ho(NO_3)_3 \cdot 5H_2O$, Sigma Aldrich, 99.99%) were used as holmium precursors. Phosphoric acid (Sigma Aldrich, 85%) and sodium phosphate monobasic (NaH_2PO_4, Sigma Aldrich $\geq$99.0%) were used as phosphate source. The following polyols were used as solvents: butylene glycol (BG, Fluka, 99.5%), ethylene glycol (EG, Sigma Aldrich, 99.8%), glycerol (Gly, Sigma Aldrich, $\geq$99.5%) diethylene glycol (DEG, Sigma, $\geq$99%).Polyacrylic acid (PAA, Sigma Aldrich, Mw 1800) was used for the NPs functionalization. Phosphate Buffered Saline (PBS, Sigma Aldrich). 3-[4,5-

dimethylthiazol-2-yl]-2,5-diphenyl tetrazolium bromide (MTT, Sigma Aldrich, ≥97.5%), 4′,6-diamidino-2-phenylindole (DAPI, Sigma Aldrich, ≥98%), and propidium iodide (PI, Sigma Aldrich, ≥94%). TO-PRO-3 Iodide and RNAse solution were purchased from Thermo Fisher. Dimethyl sulfoxide (DMSO, 99%)) was supplied by Acros organics. Dulbecco's Modified Eagle Medium (DMEM), Fetal Bovine Serum (FBS), L-glutamine and penicillin/streptomycin solution were obtained from Gibco. All chemicals were used as received, except PBS, which was applied the following procedure: one tablet of PBS was dissolved in 200 mL water to obtain 137 mM NaCl, 2.7 mM KCl and 10 mM phosphate Buffer, pH 7.4 at 25 ºC).

2.2. NPs synthesis

The HoPO$_4$NPs were obtained using a homogeneous precipitation reaction. The standard procedure was as follows. Holmium acetate was dissolved in 10 mL of butylene glycol with magnetic stirring at 70 ºC to obtain a 0.010 M solution. The solution was cooled down to room temperature and admixed with H$_3$PO$_4$ (0.15 M). This mixture was magnetically stirred for 5 minutes at room temperature to favor homogenization and aged for 1 hour in tightly closed test tubes using a microwave oven at 180 ºC. Several experiments were also conducted to analyze the effect of the synthesis parameters (solvent nature, phosphate source, H$_3$PO$_4$ and holmium concentration, aging temperature and heating source) on the characteristics of the precipitated particles.

The resulting dispersions were cooled down to room temperature, centrifuged to remove the supernatants and washed, twice with ethanol and once with double distilled water. The purified particles were finally suspended in Milli-Q water (resultant pH ~ 4) and, for some analyses, they were dried at room temperature.

2.3. NPs functionalization

The NPs were dispersed in Milli-Q water (1 mg·cm^{-3}) and the pH was adjusted to 10 with addition of NaOH. Polyacrylic acid (2 mg·cm^{-3}) was then added to the suspension and, again, the pH was again adjusted to 10 with NaOH. Finally, the resulting suspension was maintained under magnetic stirring for 1 hour at room temperature. The supernatant was subsequently removed by centrifugation at 14000 rpm for 20 minutes, and the resulting NPs were washed twice with Milli-Q water through centrifugation in the same conditions and redispersed in Milli-Q water. The pH of the resultant suspension was around 4 for all functionalized NPs.

2.4. Characterization techniques

Transmission electron microscopy (TEM) was used to examine the morphology and size of the precipitated NPs using a JEM-2100Plus microscope. Size distribution histograms were obtained from TEM micrographs using the ImageJ open source image processing program.

X-ray diffraction (XRD) patterns were recorded in a Panalytical, X´Pert Pro diffractometer (CuKα) with an X-Celerator detector over an angular range of 10º < 2θ <80º, 2θ step width of 0.03º, and 10 s counting time.

The colloidal stability of aqueous or PBS suspensions of the particles (0.5 mg·mL^{-1}) before and after functionalization was analyzed from *Dynamic Light Scattering* (*DLS*) measurements using Malvern Zetasizer Nano-ZS90 equipment, which was used as well to measure Zeta potential .

Fourier Transform Infrared (FTIR) spectra were recorded in KBr pellets of the NPs using a JASCO FT/IR-6200 equipment.

Thermogravimetry (TG) analyses were conducted in air atmosphere employing a heating rate of 10ºC·min^{-1} in a Q600 TA instrument.

Inductively Coupled Plasma High Resolution Mass Spectroscopy (ICP-HRMS). Ho concentrations in NPs and tissues were determined on an ICP-HRMS Perkin-Elmer NexION. The complete protocol is described in detail in the Supporting Information.

Relaxivity measurements. ^{1}H NMR relaxation times, T_1 and T_2, were measured at low (1.44 T), and high (9.4 T) magnetic fields, using solutions of HoPO$_4$ NPs in PBS with NPs concentrations ranging between 0.69 and 0.022 mM Ho. Low magnetic field measurements were performed on a Bruker Minispec system (Bruker BioSpin, Rheinstetten, Germany). T_1 was determined using an inversion-recovery sequence, and T_2 using the Carl-Purcell-Meiboom-Gill (CPMG) spectroscopy sequence. High magnetic field (9.4 T) measurements were performed on a Bruker Biospec MRI system (Bruker BioSpin, Ettlingen, Germany) equipped with 400 mT m^{-1} field gradients and a 40 mm quadrature bird-cage resonator. T_1 values were determined using a saturation recovery image sequence, and T_2 values using a 64-echo Carl-Purcell-Meiboom-Gill (CPMG) image sequence (TE values from 7.5 ms to 640 ms). Relaxivities, r_1 and r_2, at both

magnetic fields were calculated from the slope of the linear regression of the relaxation rate ($1/T_1$ or $1/T_2$) versus the Ho concentration.

2.5. In vitro cytotoxicity assessment

Cytotoxicity was evaluated in HFF-1 human foreskin fibroblasts by means of different assays, namely, MTT assay, life-dead assay and flow cytometry. These assays allowed the evaluation of different aspects related to cells viability such as mitochondrial activity, cell morphology, number of necrotic/late apoptotic cells, and cell cycle. Protocols are described in detail in the Supporting Information.

2.6. In vivo experiments

Animal handling. Male Balb/c mice (n = 3, ca. 22 g weight), provided by Janvier Labs, were used for the biodistribution and pharmacokinetics experiments. All experiments involving animals were performed in accordance with the ethical guidelines of our local ethical committee and consistent with national regulations for the care and use of laboratory animals (R.D. 53/2013). Before imaging studies, animals were anesthetized with isoflurane 3 % (1-1.5 mL/min) and the tail vein cannulated for the intravenous injection of NPs. Then, animals were placed into the MRI system, where they were remained anesthetized throughout the experiment (1% isoflurane, 1 mL/min). Nanoparticles were administered at a concentration of 5 mg (Ho) per kg.

In vivo Magnetic Resonance Imaging (MRI). MRI experiments were carried out on the 9.4 T Bruker Biospec system described above. High resolution T_2-weighted images were acquired using a turbo-RARE sequence with respiratory gating (TE = 16 ms, TR = 1000 ms, 4 averages, 156 □m in-plane resolution and 1 mm slice thickness). Quantitative T_2 measurements were also performed using a multi-echo spin echo sequence (TEs ranging from 7 ms to 448 ms, TR = 3500 ms, FOV = 4 cm, matrix size = 128x128, slice thickness = 1 mm). The time-courses were followed by using a dynamic turbo-RARE sequence with the same parameters indicated above, but only 1 average to improve temporal resolution (1 image every 30 seconds). The acquisition scheme was as follows: T_2-weighted, quantitative T_2, intravenous injection of the $HoPO_4$ nanoparticles, dynamic T_2-weighte sequence for 35 min, quantitative T_2, and T_2-weighted. Dynamic T_2-weigthed images were analyzed semi-quantitatively using the following expression:

$$RE = \left| \frac{I_t - I_0}{I_0} \times 100 \right|$$

where RE is the modulus of relative signal enhancement, I_t is the signal intensity at any given time after the nanoparticles injection, and I_0 is the signal intensity before the injection of NPs. Quantitative T_2 mapping was performed at 0 h and 1 h.

Finally, dynamic contrast-enhanced (DCE) MRI was also performed in tumor-bearing animals after the intravenous injection of a commercial Gd-chelate. DCE images were acquired using the following parameters: TE= 16 ms, TR = 666 ms, 1 average, 167 μm in-plane resolution and 1 mm slice thickness.

Pharmacokinetics were obtained from the dynamic studies by calculating the average signal intensity values within different regions of interest (ROIs) placed on the following tissues: liver, kidney, muscle and tumor (in the case of tumors-bearing animals).

2.7. Statistical analysis

Statistical analysis was performed using the SPSS package (v20, SPSS Inc., Chicago, Illinois). Cell viability, *in vivo* T_2, and ICP values are shown as mean ± standard deviation (SD). Student's t-test or one-way analysis of variance (ANOVA) were used to determine significant differences. The level of significance was set at $p<0.05$.

3. Results and discussion

3.1. Synthesis and physicochemical characterization of the NPs

Figure 1a shows the TEM micrographs of the NPs synthesized by aging, at 180 ºC for 1 hour, 10 mL of a BG solution containing holmium acetate (0.01 M) and H_3PO_4 (0.15 M) in a microwave oven. This procedure rendered uniform, cubic-shaped NPs, with a mean edge size of 48 nm, as inferred from the histogram shown in Figure 1b. When the H_3PO_4 concentration was halved (0.075 M), uniform NPs with cubic shape were also obtained (Figure 1c), although in this case the mean edge size was reduced to 27 nm (Figure 1d). On the other end, when the H_3PO_4 concentration was increased to 0.30 M the opposite effect was observed, with the precipitation of cubic NPs showing 80 nm edge size (Figures 1e and 1f). The NPs shown in Figures 1a, 1c and 1e will be called Ho48, Ho27 and Ho80, respectively, from now on.
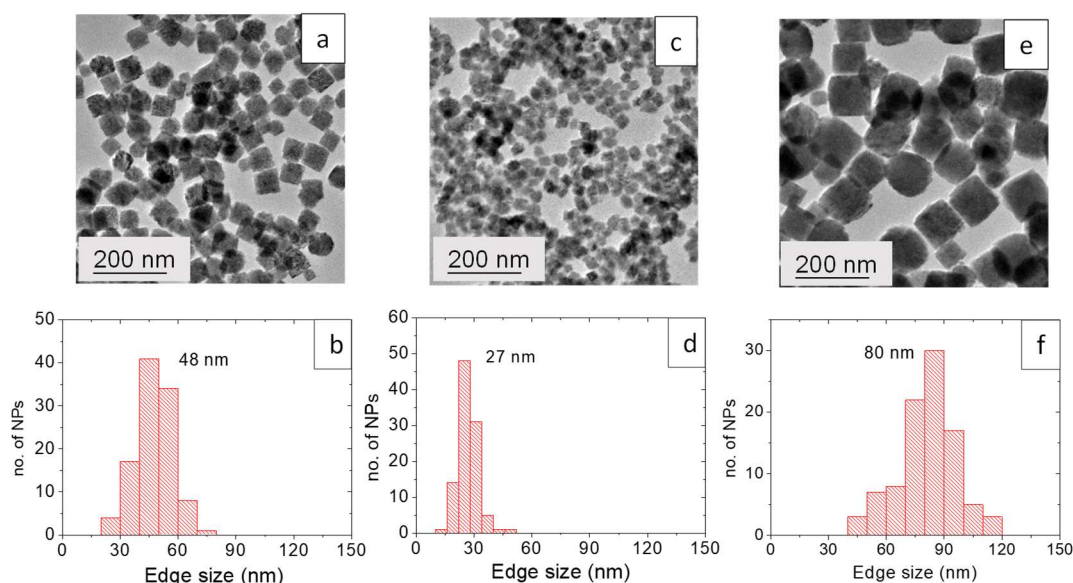
Figure 1: TEM micrographs and corresponding size distribution histograms of HoPO$_4$NPs synthesized by solvothermal reaction of butylene glycol solutions of holmium acetate (0.01 M) and different H$_3$PO$_4$ concentrations in a microwave oven at 180 ºC for 1 hour. [H$_3$PO$_4$]= 0.15 M (a and b, Ho48NPs), 0.075 M (c and d, Ho27NPs), 0.30 M (e and f, Ho80NPs).

We have subsequently analyzed the effect that the change of just one of the experimental conditions used to synthesize the Ho48 NPs, keeping the rest constant, exert on the morphology of the observed precipitates. The use of EG or Gly as solvents, instead of BG, resulted in uniform lenticular particles, with mean diameter bigger than 100 nm (122 nm and 141 nm, respectively), while the use of DEG rendered bigger particles (> 200 nm) of irregular shape (Figure S1). The phosphate source was also essential to obtain uniform NPs, as the change of H$_3$PO$_4$toNaH$_2$PO$_4$ rendered an irregular precipitate (Figure S2a). A similar effect over the morphology of the resulting precipitate had the change of the holmium concentration from 0.01 M to 0.02 M, as observed in FigureS2b. Changing the heating source from microwaves to conventional heating was not as drastic as the changes reported above, but it produced less regular and bigger NPs (Figure S2c) compared to those of Figure 1a. Finally, other parameters like the aging temperature (120ºC) or the holmium precursor (nitrate) did not have a significant effect on the morphology of the precipitated NPs, as observed in Figures S3a and S3b, respectively. All the observed effects must be assigned to variations in the kinetics of precipitation induced when altering the experimental conditions, which affect the nucleation and growth processes.[27] The critical experimental conditions for the formation of HoPO$_4$ nano-sized, uniform particles could explain the scarce number of papers found in the literature dealing with the study of this type of material and highlights the importance of this finding.

Following is the structural characterization of the three types of NPs shown in Figure 1 as well as the study of their colloidal stability in PBS. The XRD patterns (Figure 2) exhibited, exclusively, the reflections corresponding to tetragonal $HoPO_4$ (PDF 01-076-1533) over a flat background, indicating the absence of any other crystalline or amorphous phases and the purity of the samples. The crystallite size, estimated from the width of the reflection located at ~35 º2θ using the Scherrer formula, was 31 nm, 52 nm and 85 nm for the Ho27, Ho48 and Ho80 NPs, respectively. The proximity of the crystallite size and the particle edge in each case suggests the single crystal character of all three types of NPs.
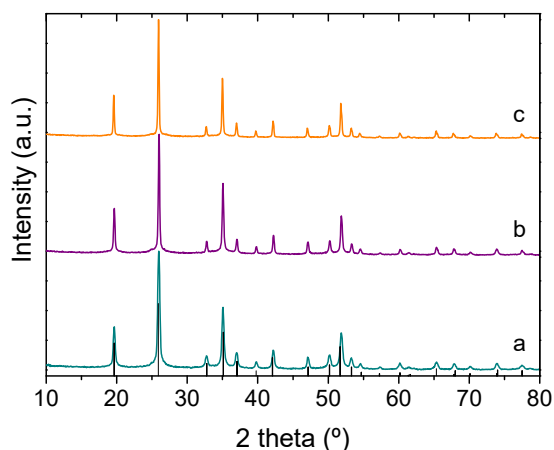
Figure 2: XRD patterns of Ho27 (a), Ho48 (b) and Ho80 (c) NPs. Ticks at the bottom of the graph correspond to tetragonal $HoPO_4$ (PDF 01-076-1533).

The colloidal stability of the three types of NPs dispersed in both water (pH ~ 4) and PBS was analyzed using DLS (Table 1).

Table 1: Mean hydrodynamic diameter (HD) values of the $HoPO_4$ NPs in water and PBS before and after functionalization with PAA obtained from DLS measurements. The value in parenthesis is the polydispersity index (PDI) obtained in the same measurement.

Sample	HD in H_2O (pH ~4)		HD in PBS	
	As-synthesized	@PAA	As-synthesized	@PAA
Ho27	320 nm	100 nm (0.32)	890 nm	250 nm (0.26)
Ho48	417 nm	160 nm (0.13)	950 nm	140 nm (0.14)
Ho80	605 nm	175 nm (0.10)	2000 nm	190 nm (0.07)

The high values of the mean hydrodynamic diameter obtained for the as-synthesized NPs in water and PBS indicated that the NPs were aggregated in both solvents, the degree of

aggregation in PBS being considerably higher than in water as a consequence of the effect of the high ionic strength of the buffer. In order to increase the colloidal stability of the NPs, they were submitted to a functionalization process with poly(acrylic) acid (PAA) following the method described in the experimental section. The effective coating with the carboxylate groups provided by the PAA was then confirmed with the help of FTIR spectra and TG curves. The FTIR spectrum of the Ho48 NPs after the functionalization process is shown in Figure 3a, together with that of the as-synthesized NPs. Both spectra were very similar to one another, showing all active IR modes corresponding to the stretching and bending vibrations of the phosphate group at <1200 cm^{-1},[28] as well as the bands at 3420 cm^{-1} and 1635 cm^{-1} due to adsorbed water.[29] In addition, both spectra showed a low intensity band at ~1400 cm^{-1} (marked with an asterisk) that can be assigned to C-H bending vibrations, suggesting the presence of some solvent moieties adsorbed on the particles surface. The spectrum of the functionalized NPs exhibited, as a distinctive feature, a band at ~1550 cm^{-1} (marked with an arrow and magnified in the inset); this band, which is characteristic of carboxylate groups, indicated the presence of such groups on the NPs surface and confirmed the success of the functionalization process.[30] Similar FTIR spectra were obtained for the Ho27 and Ho80 NPs before and after functionalization with PAA (Figure S4), which likewise indicated the effective coating of the particles with carboxylate groups of the PAA. Thermogravimetric analyses were recorded to estimate the amount of PAA attached to the surface of the functionalized NPs. The TG curves corresponding to the Ho48 NPs before and after functionalization (Figure 3b) showed two well differentiated weight losses. The first one, between room temperature and ~250 ºC, was very similar in both samples and it is due to the release of water (~4 wt%) while the second one, from ~250 ºC to 800 ºC is associated with the decomposition of adsorbed organic species. This second loss can be assigned to solvent moieties in the case of the as-synthesized NPs (accounting for 1.5 wt%), while in the functionalized NPs such loss was higher (3 wt%) and must be attributed to both, the decomposition of solvent species and carboxylate groups. Therefore, it can be concluded that the amount of PAA species on the surface of the Ho48 functionalized NPs corresponds to 1.5 wt%. Similar TG curves were observed for the Ho27 and Ho80 NPs before and after the functionalization process (Figure S5). The hydrodynamic diameter values measured on aqueous and PBS suspensions of the functionalized NPs are shown in Table 1. A significant decrease is observed for all values when compared with the particles before functionalization, which demonstrates the utility of the PAA coating on the colloidal stability of the NPs.
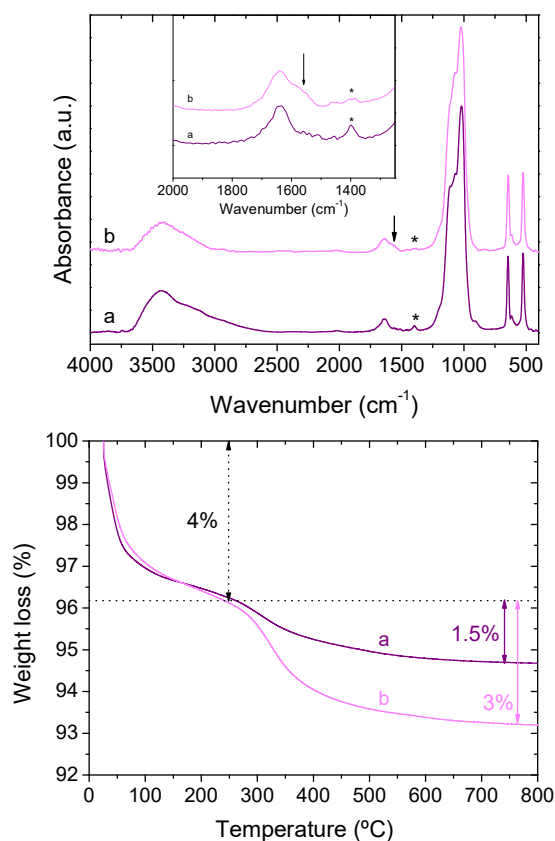
Figure 3: Top: FTIR spectra of Ho48 NPs (a) and Ho48@PAA NPs (b). Bottom: Thermogravimetry curves of Ho48 NPs (a) and Ho48@PAA NPs.

3.2. In vitro characterization of the NPs: Magnetic relaxivity of the NPs

Phantom MR images of the functionalized Ho27, Ho48 and Ho80 NPs in water at 9.4 T as a function of Ho concentration are shown in Figure 4a. The T_2-weihted MR images become darker as the NPs concentration increases for all three samples, which indicates that the NPs behave as negative MRI CAs. Figures 4b and 4c show the transverse relaxation rate ($1/T_2$) as a function of holmium concentration at 1.44 T and 9.4 T, respectively, for the functionalized Ho27, Ho48 and Ho80 NPs in water. The data could be successfully fitted to a line in each case, and the slopes of the lines provided the corresponding r_2 values (Table 2). The r_1 values were similarly obtained from the slope of the $1/T_1$ vs. [Ho] curves and they are summarized as well in Table 2. The r_2 values are very high compared to the r_1 ones at both low and high magnetic fields, as expected for negative CAs. This is due to the magnetic characteristics of the Ho^{3+} ion, with strong magnetic anisotropy and fast electronic relaxation rate, whose interaction with the nuclear spins of the protons results predominantly in the shortening of the transverse relaxation time (T_2) at any field strength.[9] It can be observed in Table 2 that the r_2 values increase

with increasing NPs size at 1.44 T, while at 9.4 T this trend fails for the largest NPs (Ho80). It should be noticed, however, that some aggregation was observed in Ho80 NPs at 9.4 T, which means that the measured r_2 is most likely underestimated. Therefore, we can assume that the positive correlation between r_2 and particle size also holds for high magnetic fields. In addition, the r_2 values at high field are much higher than at low magnetic field. These results can be explained on the basis of the paramagnetic relaxation enhancement (PRE), which is the interaction of lanthanides with the proton spins. PRE can be expressed as the sum of three components, namely contact, dipolar and Curie terms, the latter being predominant for lanthanides other than Gd^{3+}. The Curie component mainly depends on spins correlation times and on the square of the applied magnetic field strength. The dependence with the spin correlation time explains the linear increase of r_2 with the NP size. As described by Yung et al.,[31] in a system composed of randomly distributed stationary magnetic spheres ($HoPO_4$ NPs, in our case) surrounded by proton spins (hydrogen nuclei of water) undergoing unrestricted, isotropic diffusing motion, two frequency scales are present, each characterizing one underlying relaxation mechanism: the dynamic frequency scale and the magnetic frequency scale. The dynamic frequency scale specifies how fast the spins are relaxed by the magnetic spheres the spins encounter as they move about, while the magnetic frequency scale specifies how fast the spins are relaxed by the local field inhomogeneity of one nearby magnetic sphere. For small NPs with a radius of a few nanometers, as those reported in this study, the relaxation behavior of the spin-sphere system falls into the outer sphere regime, i.e., the dynamic frequency scale dominates over the magnetic frequency scale because the spins diffusion is faster than the spatial variation of the local field inhomogeneities produced by a single particle. Given that the dynamic frequency scale is the inverse of the translational correlation time τ ($\tau = r^2/D$, where r is some characteristic dimension of the NP and D is the diffusion coefficient of water), this eventually results in the linear increase of r_2 with the particle dimension. Such increase in transverse relaxivity with increasing nanoparticle size has been observed in other nanoparticulated systems such as HoF_3,[22] $NaHoF_4$,[20] $NaDyF_4$,[15,18] and Dy_2O_3[14] and it is also observed in Table 2 for the NPs studied in this paper, with the exception commented above.

The Curie component depends as well on the square of the applied magnetic field strength so that the Curie spin relaxation would be responsible for an increment of the T_2 relaxivity of our NPs by a factor of 42.6 as the field goes up from 1.44 T to 9.4 T. The r_2 values in

Table 2 are in good agreement with this dependence for the smallest NPs, while a slight deviation is observed for the intermediate size NPs, the largest NPs being an order of magnitude away from this dependence very likely due to the aggregation observed for these big NPs under the 9.4 T field, as explained above.
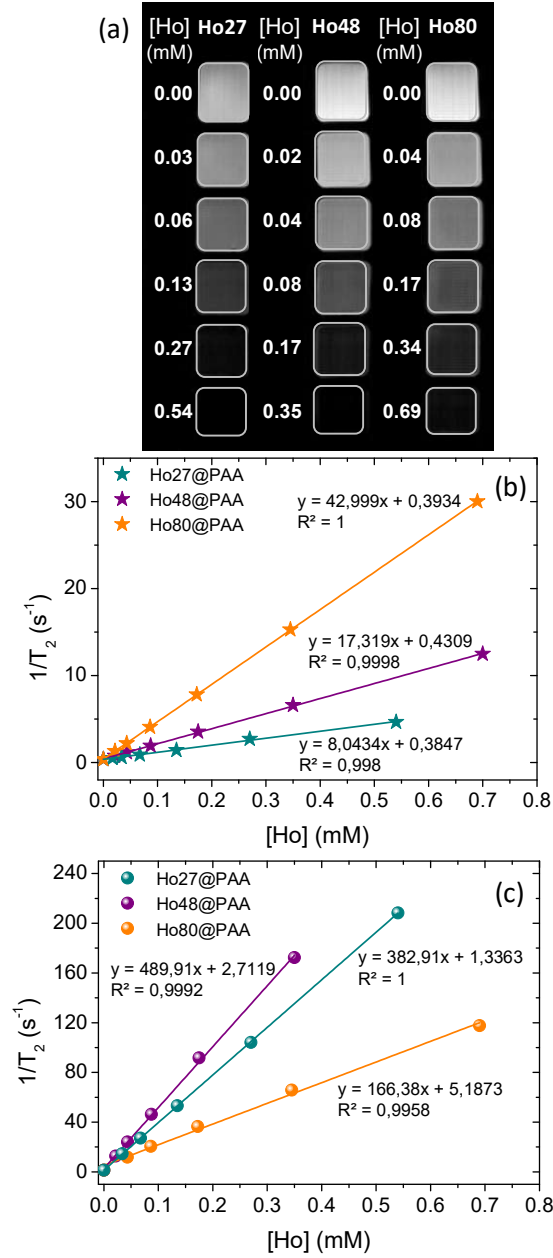
Figure 4: a) Concentration dependent phantom image contrast of the Ho27@PAA, Ho48@PAA and Ho80@PAA NPs at 9.4 T. T_2 relaxation rates as a function of Ho concentration in aqueous suspensions of Ho27@PAA, Ho48@PAAand Ho80@PAA at 1.44 T (b)and 9.4 T (c).

Table 2: Longitudinal (r_1) and transverse (r_2) relaxivity values at 1.44 T and 9.4 T of the HoPO$_4$ NPs functionalized with PAA.

Sample	1.44 T		9.4 T	
	r1	*r2*	*r1*	*r2*
Ho27@PAA	0.062	8.043	0.100	382.91
Ho48@PAA	0.066	17.319	0.251	489.91
Ho80@PAA	0.035	42.999	0.089	166.38

Sample Ho48 showed the highest r_2 value (489.9 mM^{-1}s^{-1}) at 9.4 T among the three samples analyzed in this study. This is also, to the best of our knowledge, the highest value of r_2 reported in the literature for Holmium-based NPs,[18,20,21,32,33] except for HoF$_3$ NPs that showed an r_2 value of 608.39 mM^{-1}s^{-1} at 9.4 T.[22] Sample Ho48 has been consequently selected for *in vivo* experiments.

3.3. Cytotoxicity Assays

Cellular toxicity of Ho48 was assessed in HFF-1 human foreskin fibroblasts. Different parameters were tested for a complete evaluation of the cytotoxic response, including cell morphology, induction of necrotic/late apoptotic cells, mitochondrial activity and cell cycle. Microscopy images obtained by merging brightfield, DNA staining (DAPI), and nuclei staining (TO-PRO-3 Iodine), show that the exposure of cells to Ho48 NPs, even at the highest concentration tested (100 µg/mL Ho), did not produce any appreciable morphological change (Figure 5a-c). Cellular necrosis was evaluated by counting the total number of cells in the "live-dead" assay (Figure 5d). No statistically significant decrease ($p<0.05$) in cell number was observed for any of the concentrations tested, i.e., no evidence of necrosis was found. Similarly, no statistically significant difference ($p <0.05$) was observed between cells exposed to any concentration of NPs and negative control cells, meaning that there were no apoptotic cells (Figure 5e). Mitochondrial activity was also not affected by the presence of NPs, at any of the concentrations tested, as indicated by the MTT analysis shown in Figure 5f. Moreover, flow cytometry analysis of sub-G1 phase further supported the absence of apoptosis. Apoptotic cells exhibit specific morphological features like cell shrinkage, organelles tightly packed, as well as chromatin condensation. These characteristics promote the appearance of the sub-G1 phase population in cell cycle analysis by flow cytometry.[34] As shown in Figure 5, the

percentage of cells in sub-G1 phase remained unchanged as the concentration of Ho48 NPs increased (Figure 5g-i), that is, the presence of NPs did not induce apoptosis at any of the concentrations tested.
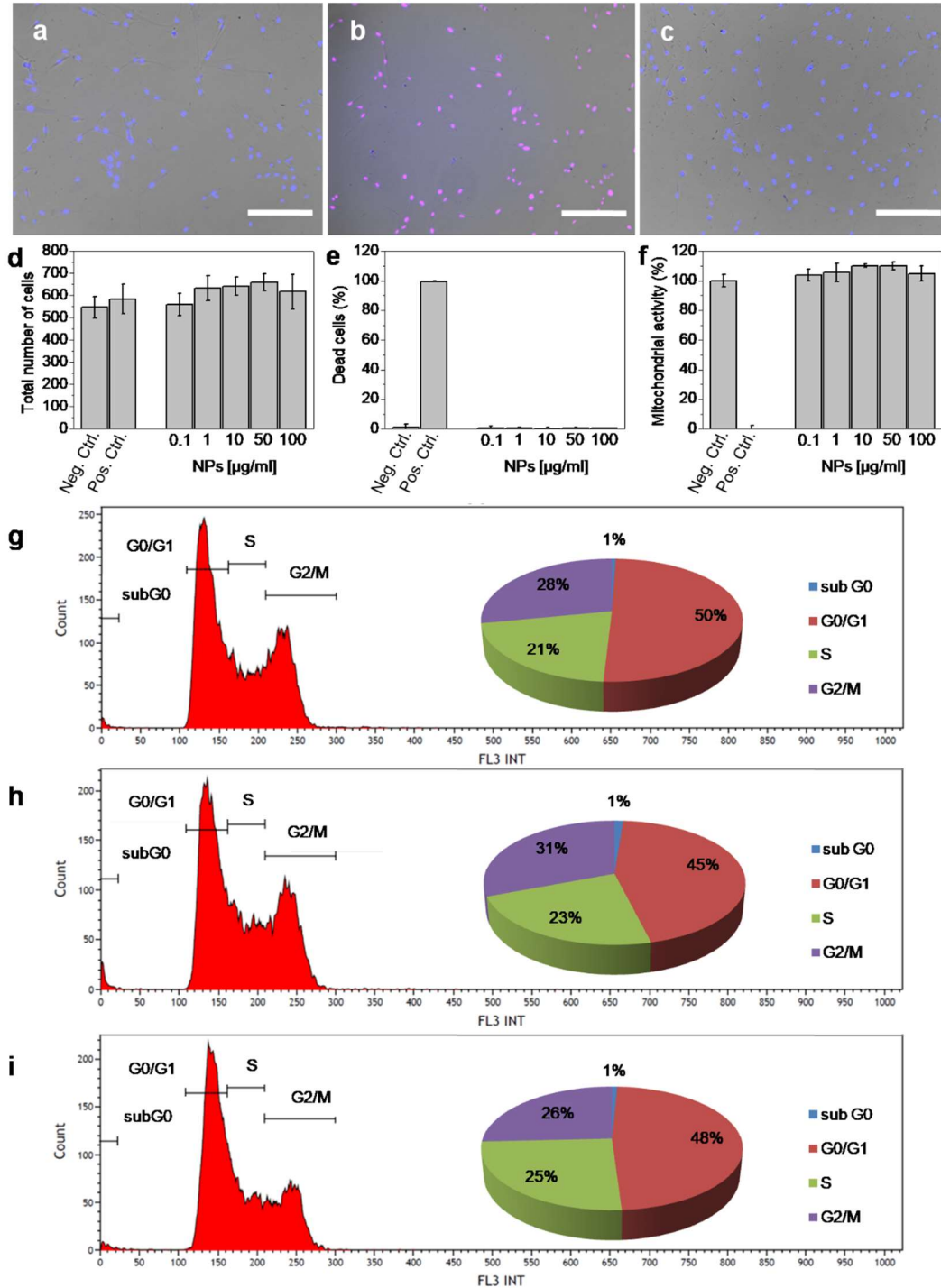

Figure 5: Optical microscopy images of HFF-1 fibroblasts resulting from the merge of bright field (grey), DAPI (blue) and TO-PRO-3 Iodine (red) images: a) negative control, b) positive control, c) cells exposed to 100 μg/ml Ho of Ho48. Scale bar corresponds to 50 μm. Total number of cells per well after exposure to increasing concentration of Ho48 NPs (d). Percentage of dead cells after exposure to increasing concentration of Ho48 NPs (e). MTT assay of cells exposed to increasing concentration of Ho48 NPs (f). Tested concentrations were from 0.1 μg/ml to 100 μg/ml Ho. Flow cytometry analysis of cell cycle after 24 h of treatment with 0 μg/ml (h), 10 μg/ml (h) and 100 μg/ml (i) of Ho48 NPs.

3.4. Biodistribution and pharmacodynamics in control mice

3.4.1. In vivo MRI

Once the absence of cytotoxic effects was verified, Ho48NPs were studied *in vivo* as potential CAs for MRI. Dynamic MRI experiments (Figure 6a) showed a rapid increase of the relative enhancement (RE) in liver and spleen, around 50% and 25%, respectively, within the first 5 minutes after injection of Ho48 NPs, and then the RE values remained stationary during the rest of the experiment. These *in vivo* pharmacokinetic profiles indicated that Ho48 NPs are readily recognized by the mononuclear phagocyte system (MPS), leading to rapid clearance from the bloodstream by liver kupffer cells and splenic macrophages. On the other hand, kidneys exhibited a rapid increase right after the injection (20% RE approximately), followed by a fast decrease to near basal levels, indicating that Ho48 NPs are not retained in these organs, which is in good agreement with previously reported findings for NPs of similar hydrodynamic diameter.[35] Accordingly, high-resolution T_2-weigthed images acquired before and 1h after the injection of Ho48 NPs showed a clear darkening of both liver and spleen, while almost no signal change could be observed in the kidneys (Figure 6b). These results were further confirmed by quantitative T_2 mapping at 0 and 1h post injection, which showed large and statistically significant decrease ($p<0.05$) of T_2 in the liver ($\Delta T_2=7.0$ms) and spleen ($\Delta T_2=4.3$ms), and a slight decrease in the kidneys ($\Delta T_2=2.3$ ms) (Figure 6c).
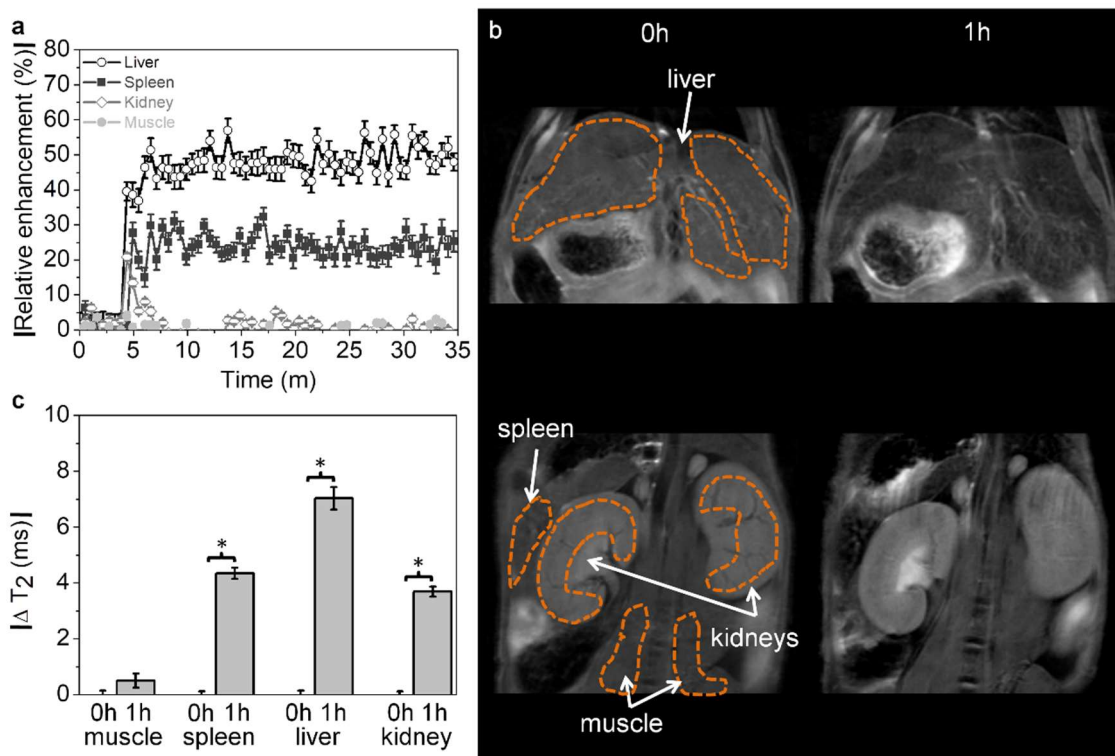
Figure 6: a) In vivo time courses of Ho48 after being intravenously injected in mice: Muscle, Liver; Kidneys and Spleen. b) Representative T_2-weighted MR images at different experimental times after the intravenous injection of Ho48. c) ΔT_2 values of different organs at different times after intravenously injection of Ho48. The average values were obtained by performing three experiments. Dashed lines show representative ROIs used to calculate the T_2 values.

3.4.2. Quantitative ICP-MS of tissue samples

Biodistribution of Ho48 NPs was studied by ICP-MS quantitative analysis of Ho content in liver, spleen, kidneys, lungs, brain and blood. Figure 7 shows the absolute concentrations in the different organs (Figure 7a), and the percentage with respect to the total injected Ho (Figure 7b). The concentration of Ho in the liver 1 h after intravenous injection of Ho48 NPs was 100.1 μg of Ho/g of dry tissue, which corresponds to 39.6 % of the injected Ho. Spleen also showed high concentration of NPs at this time (64.9 μg of Ho/g of dry tissue), although it only represents 1.9 % of the injected Ho due to its small size compared to the liver. Concentrations in the rest of organs were much lower, with 15.3 μg/g of dry tissue in the lungs, 0.6 μg/g of dry tissue in the kidneys, and almost undetectable amounts in the brain. As for blood, Ho levels were undetectable in all cases. The large amount of Ho in liver and spleen, together with the fact that no Ho could be

detected in the blood, demonstrate the rapid and avid uptake of Ho48 NPs by the MSP, as suggested by the MRI findings.
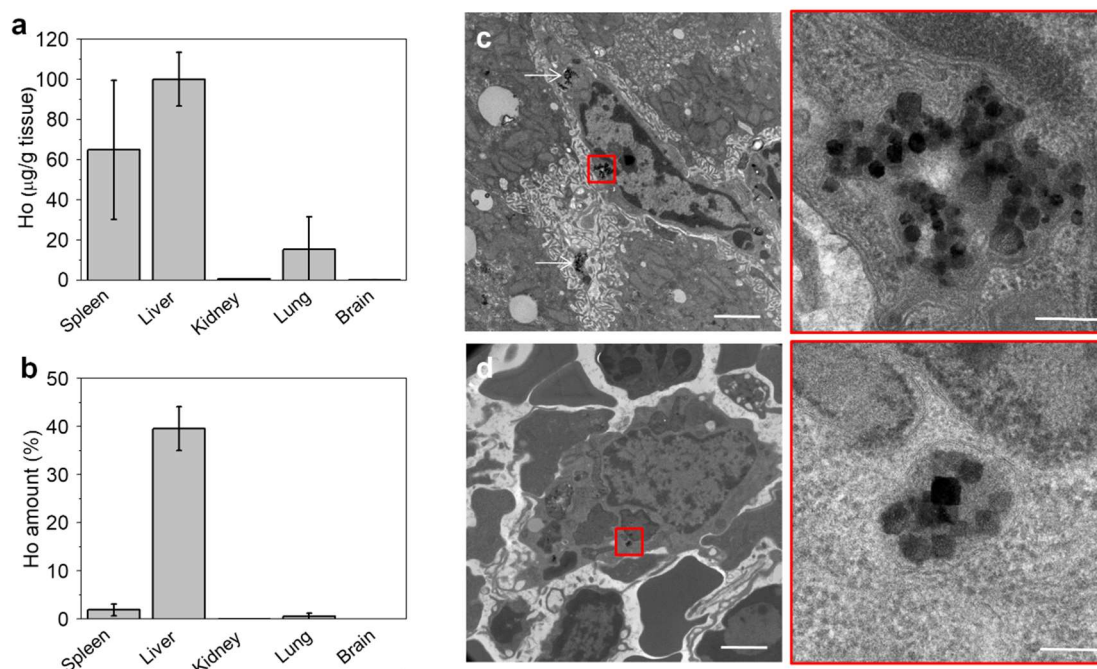
Figure 7: Biodistribution of intravenously injected Ho48 NPs quantified by ICP−MS in absolute values (a) and relative to the total amount of injected Ho (b). Tissue samples were taken 1h after intravenous injection of Ho48 NPs to Balb/c mice (n = 3). TEM images of liver (c), spleen (d) tissues collected at 1 hour after the intravenous administration of Ho48 NPs. Scale bar correspond to 2 μm (inset: 200 nm). Error bars represent standard deviation of the mean value (n=3).

3.4.3. Ex vivo TEM

Post-mortem samples were also analyzed by TEM, which confirmed the presence of Ho48 NPs in liver and spleen. NPs in spleen resembled original NPs, with similar shape and size (Figure 7d). In contrast, NPs in the liver, showed a more spherical shape and smaller size (Figure 7c), suggesting partial degradation. Also, as expected, Ho48 NPs in the liver accumulated into the kupffer cells. These results further confirmed the in vivo MRI and the ICP-MS findings, showing a preferential and high accumulation of Ho48 NPs in liver and spleen.

In summary, Ho48 NPs showed outstanding properties as potential MRI contrast agents, with extremely large magnetic relaxivity at high field, along with the absence of cytotoxicity. Thus, when injected in vivo, even at the low concentration of 5 mg (Ho)/Kg, they were able to induce a drastic signal drop in T_2-weighted MR images. On the downside, these NPs were rapidly recognized and cleared from the bloodstream by the MPS. This behavior is not surprising, as it is well known that NPs between 15 and 200

nm are typically taken up by Kupffer cells and splenic macrophages,[36] and Ho48 NPs fall within this size range, with and HD of 140 nm in physiological medium. However, recognition by the MPS not only depends on the size of NPs, but also on many other factors, such as coating, shape or surface charge.[37,38] Therefore, the use of other coatings to improve the stealth properties of this NPs is currently under investigation in our group.

4. Conclusions

We have successfully synthesized cubic-shaped $HoPO_4$ nanoparticles, from H_3PO_4 and holmium acetate, by homogeneous precipitation in butylene glycol. Nanoparticles with three different sized (27 nm, 48 nm and 80 nm) were obtained by simply changing the H_3PO_4 concentration used. The nanoparticles, consisting of tetragonal $HoPO_4$ single crystals, were easily functionalized with poly(acrylic) acid and showed good colloidal stability in physiological medium (PBS). Relaxivity measurements performed at both 1.5 T and 9.4 T showed r_2 values much higher than the r_1 ones for all three nanoparticle types, which indicated that the $HoPO_4$ NPs behave as negative MRI contrast agents. It can also be concluded that positive correlation between r_2 and particle size takes place for both low and high magnetic fields, while the r_2 values observed at high field were much higher than at low field. Among the three nanoparticles studied, those with 48 nm cube edge showed the one of the highest r_2 value (489.9 $mM^{-1}s^{-1}$) at 9.4 T reported in the literature.[18,20] A comprehensive cytotoxicity evaluation in cultured human fibroblasts showed that Ho48 NPs did not cause any significant toxic effect even at the very high concentration of 100 μg/ml. Finally, *in vivo* studies demonstrated the great potential of these NPs as high field T_2 MRI contrast agents. Further studies are underway to determine the feasibility of NPs bioconjugation and to analyze their relative enhancement in tumors using dynamic MRI experiments.

Sample CRediT author statement

E. Gómez-González: Investigation, Formal analysis. **Carlos Caro:** Investigation, Formal analysis, **D. Martínez-Gutiérrez:** Investigation. **María L. García-Martín:** Writing - Original Draft, Supervision, Funding acquisition. **M. Ocaña:** Supervision, Project administration, Funding acquisition. **A. I. Becerro:** Writing - Original Draft, Review & Editing, Supervision, Funding acquisition.

Acknowledgements

References

1 J. Lohrke, T. Frenzel, J. Endrikat, F. Caseiro Alves, T. M. Grist, M. Law, J. Min Lee, T. Leiner, K.C. Li, K. Nikolaou, M. R. Prince, H. H. Schild, J. C. Weinreb, K. Yoshikawa, H. Pietsch. 25 Years of Contrast-Enhanced MRI: Developments, Current Challenges and Future Perspectives. *Adv. Ther.,* 2016, **33**, 1–28.

2 H. Dong, S. R. Du, X. Y. Zheng, G. M. Lyu, L.D. Sun, L. D. Li, P. Z. Zhang, C. Zhang, C. H. Yan. Lanthanide Nanoparticles: From Design toward Bioimaging and Therapy. *Chem. Rev.*, 2015, **115**, 10725−10815.

3 A. Escudero, A. I. Becerro, C. Carrillo-Carrion, N. O. Nuñez, M. V. Zyuzin, M. Laguna, D. Gonzalez-Mancebo, M. Ocaña, W. J. Parak. Rare earth based nanostructured materials: synthesis, functionalization, properties and bioimaging and biosensing applications. *Nanophotonics*, 2017, **6**, 881-921.

4 N. Hoshyar, S. Gray, H. Han, G. Bao. The effect of nanoparticle size on in vivo pharmacokinetics and cellular interaction. *Nanomedicine (Lond),* 2016, **11**, 673–692.

5 Y. Xiao, J. Du. Superparamagnetic nanoparticles for biomedical applications. *J. Mater. Chem. B*, 2020, **8**, 354–367.

6 J. T. Rosenberg, J. M. Kogot, D. D. Lovingood, G. F. Strouse, S. C. Grant. Intracellular Bimodal Nanoparticles Based on Quantum Dots for High-Field MRI at 21.1 T. *Magn. Res. Med.,* 2010, **64**, 871–882.

7 M. Rohrer, H. Bauer, J. Mintorovitch, M. Requardt, H. J. Weinmann. Comparison of magnetic properties of MRI contrast media solutions at different magnetic field strengths. *Invest. Radiol.* 2005, **40**, 715

8 G. Pintacuda, M. John, X. C. Su, G. Otting. NMR Structure Determination of Protein-Ligand Complexes by Lanthanide Labeling. *Acc. Chem. Res.,* 2007, **40**, 206–212.

9 M. Norek, J. A. Peters. MRI Contrast Agents Based on Dysprosium or Holmium. *Prog. Nucl. Magn. Reson. Spectrosc.*, 2011, **59**, 64−82.

10 P. Caravan, M. T. Greenfield, J. W. M. Bulte. Molecular Factors That Determine Curie Spin Relaxation in Dysprosium Complexes. *Mag. Res. Med.,* 2001, **46**, 917–922.

11 M. Harris, C. Henoumont, W. Peeters, S. Toyouchi, L. V. Elstband, T. N. Parac-Vogt. Amphiphilic complexes of Ho(III), Dy(III), Tb(III) and Eu(III) for optical and high field magnetic resonance imaging. *Dalton Trans.*, 2018, **47**, 10646-10653.

12 S. Aime, M. Botta, L. Barbero, F. Uggeri, F. Fedeli. Water signal suppression by T2-relaxation enhancement promoted by Dy(III) complexes. *Magn. Reson. Chem.,* 1991, **29**, S85–S88.

13 C. Todd, S. Soesbe, J. Ratnakar, M. Milne, S. Zhang, Q. N. Do, Z. Kovacs, A. D. Sherry. Maximizing T2-Exchange in Dy(3+)DOTA-(amide)X Chelates: Fine-Tuning the Water Molecule Exchange Rate for Enhanced T2 Contrast in MRI. *Magn. Res. Med.*, 2014, **71**, 1179–1185.

14 M. Norek, E. Kampert, U. Zeitler, J. A. Peters. Tuning of the size of Dy_2O_3 nanoparticles for optimal performance as an MRI contrast agent. *J. Am. Chem. Soc.*, 2008, **130**, 5335–5340.

15 G. K. Das, N. J. J. Johnson, J. Cramen, B. Blasiak, P. Latta, B. Tomanek, F. C. J. M. van Veggel. $NaDyF_4$ nanoparticles as T_2 contrast agents for ultrahigh field magnetic resonance imaging. *J. Phys. Chem. Lett.*, 2012, **3**, 524.

16 Y. Zhang, V. Vijayaragavan, G. K. Das, K. K. Bhakoo, T. T. Y. Tan. Single-phase $NaDyF_4$:Tb^{3+} nanocrystals as multifunctional contrast agents in high-field magnetic resonance and optical imaging. *Eur. J. Inorg. Chem.*, 2012, 2044–2048.

17 Y. Zhang, G. K. Das, V. Vijayaragavan, Q. C. Xu, P. Padmanabhan, K. K. Bhakoo. Smart" theranostic lanthanide probes with simultaneous up-conversion fluorescence and tunable T_1-T_2 magnetic resonance imaging contrast and near-infrared activated photodynamic therapy. *Nanoscale,* 2014, **6**, 12609–12617.

18 X. Zhang, B. Blasiak, A. J. Marenco, S. Trudel, B. Tomanek, F. C. J. M. van Veggel. Design and regulation of $NaHoF_4$ and $NaDyF_4$ nanoparticles for high-field magnetic resonance imaging. *Chem. Mater.*, 2016, **28**, 3060–3072.

19 Y. Li, Y. Y. Gu, W. Yuan, T. Y. Cao, K. Li, S. P. Yang, Z. G. Zhou, F. Y. Li. Core-shell-shell $NaYbF_4$:Tm@CaF_2@$NaDyF_4$ nanocomposites for up-conversion/T_2-weighted MRI/Computed tomography lymphatic imaging. *ACS Appl. Mater. Interfaces,* 2016, **8**, 19208–19216.

20 D. Ni, J. Zhang, W. Bu, C. Zhang, Z. Yao, H. Xing, J. Wang, F. Duan, Y. Liu, W. Fan, X. Feng, J. Shi. PEGylated $NaHoF_4$ nanoparticles as contrast agents for both X-ray computed tomography and ultra-high field magnetic resonance imaging. *Biomaterials*, 2016, **76**, 218–225.

21 Y. Feng, Q. Xiao, Y. Zhang, F. Li, Y. Li, C. Li, Q. Wang, L. Shi, H. Lin. Neodymium-doped NaHoF4 nanoparticles as near-infrared luminescent/T2-weighted MR dual-modal imaging agents *in vivo*. *J. Mater. Chem., B*, 2017, **5**, 504–510.

22 D. González-Mancebo, A. I. Becerro, T. C. Rojas, M. L. García-Martín, J. M. de la Fuente, M. Ocaña. HoF_3 and DyF_3 Nanoparticles as Contrast Agents for High-Field Magnetic Resonance Imaging. *Part. Part. Syst. Charact.*, 2017, **34**, 1700116.

23 S. Marasini, H. Yue, S. L. Ho, K. H. Jung, J. A. Park, H. Cha, A. Ghazanfari, M. Y. Ahmad, S. Liu, Y. J. Jang, X. Miao, K. S. Chae, Y. Chang, G. H. Lee. D-Glucuronic Acid-Coated Ultrasmall Paramagnetic Ln_2O_3 (Ln = Tb, Dy, and Ho) Nanoparticles: magnetic Properties, Water Proton Relaxivities, and Fluorescence Properties. *Eur. J. Inorg. Chem.*, 2019, 3832–3839.

24 H. Itoh, H. Hachiya, M. Tsuchiya, Y. Suzuki, Y. Asano. Determination of solubility products of rare earth fluorides by fluoride ion-selective electrode. *Bull. Chem. Soc. Jpn.*, 1984, **57**, 1689–1690.

25 F. H. Firsching, S. N. Brune. Solubility products of the trivalent rare-earth phosphates. *J. Chem. Eng. Data*, 1991, **36**, 93–95.

26 A. Lebugle, F. Plle, C. Charvillat, I. Rousselot, J. Y. Chane-Ching. Colloidal and monocrystalline Ln^{3+} doped apatite calcium phosphate as biocompatible fluorescent probes. *Chem. Comm.*, 2006, 606–608.

27 V. LaMer, R. Dinegar. Theory, production and mechanism of formation of monodispersed hydrosols. *J. Am. Chem. Soc.*, 1950, **72**, 4847–4854.

28 S. Lucas, E. Champion, D. Bregiroux, D. Bernache-Assollant, F. Audubert. Rare earth phosphate powders $REPO_4·nH_2O$ (RE=La, Ce or Y)—Part I. Synthesis and characterization. *J. Solid State Chem.*, 2004, **177**, 1302–1311.

29 Y. Gao, M. Fan, Q. Fang, B. Song, W. Jiang, *J. Nanosci. Nanotechnol.*, 2013, **13**, 6644–6652.

30 N. O. Nuñez, S. Rivera, D. Alcántara, J. M. de la Fuente, J. García-Sevillano, M. Ocaña. Surface modified Eu:$GdVO_4$ nanocrystals for optical and MRI imaging. *Dalton Trans.* 2013, **42**, 10725-10734.

31 K. T. Yung. Empirical models of transverse relaxation for spherical magnetic perturbers. *Magn. Reson. Imag.*, 2003, **21**, 451–463.

32 Q. L. Vuong, S. V. Doorslaer, J. L. Bridot, C. Argante, G. Alejandro, R. Hermann, S. Disch, C. Mattea, S. Stapf, Y. Gossuin. Paramagnetic nanoparticles as potential MRI contrast agents: characterization, NMR relaxation, simulations and theory. *Magn Reson. Mater. Phy.*, 2012, **25**, 467–478.

33 S. S. Syamchand, S. George. The upconversion luminescence and magnetism in Yb^{3+}/Ho^{3+} co-doped LaF$_3$ nanocrystals for potential bimodal imaging. *J. Nanopart. Res.*, 2016, **18**, 385–389.

34 C. Vignon, C. Debeissat, M. T. Georget, D. Bouscary, E. Gyan, P. Rosset, O. Herault. Flow Cytometric Quantification of All Phases of the Cell Cycle and Apoptosis in a Two-Color Fluorescence Plot. *PLoS One*, 2013, **8**, e68425.

35 C. H. J. Choi, J. E. Zuckerman, P. Webster, M. E. Davis. Targeting kidney mesangium by nanoparticles of defined size. *PNAS*, 2011, **108**, 6656–6661.

36 M. Cataldi, C. Vigliotti, T. Mosca, M. R. Cammarota, D. Capone. Emerging Role of the Spleen in the Pharmacokinetics of Monoclonal Antibodies, Nanoparticles and Exosomes. *Int. J. Mol. Sci.*, 2017 **18**, 1249.

37 M. Pernia Leal, C. Caro, M. L. García-Martín. Shedding light on zwitterionic magnetic nanoparticles: limitations for in vivo applications. *Nanoscale*, 2017, **9**, 8176–8184.

38 N. Feliu, D. Docter, M. Heine, P. Pino, S. Ashraf, J. Kolosnjaj-Tabi, P. Macchiarini, P. Nielsen, D. Alloyeau, F. Gazeau, R.H. Stauber, W. J. Parak. In vivo degeneration and the fate of inorganic nanoparticles. *Chem. Soc. Rev.*, 2016, **45,** 2440–2457.